

Article

Wind Pressure Orthogonal Decomposition Anemometer: A Wind Measurement Device for Multi-Rotor UAVs

Tianhao Hou ^{1,2}, Hongyan Xing ^{1,2,*} , Wei Gu ^{1,2}, Xinyi Liang ^{1,2}, Haoqi Li ^{1,2} and Huaizhou Zhang ^{1,2}

¹ School of Electronics Information Engineering, Nanjing University of Information Science & Echnology, Nanjing 210044, China; 20211118004@nuist.edu.cn (T.H.); 20211249294@nuist.edu.cn (X.L.)

² Jiangsu Key Laboratory of Meteorological Observation and Information Processing, Nanjing University of Information Science & Technology, Nanjing 210044, China

* Correspondence: xinghy@nuist.edu.cn

Abstract: Wind speed and direction are critical meteorological elements. Multi-rotor unmanned aerial vehicles UAVs are widely used as a premium payload platform in meteorological monitoring. The meteorological UAV is able to improve the spatial and temporal resolution of the elements collected. However, during wind measurement missions, the installed anemometers are susceptible to interference caused by rotor turbulence. This paper puts forward a wind pressure orthogonal decomposition (WPOD) strategy to overcome this limitation in three ways: the location of the sensors, a new wind measurement method, and supporting equipment. A weak turbulence zone (WTZ) is found around the airframe, where the turbulence strength decays rapidly and is more suitable for installing wind measurement sensors. For the sensors to match the spatial structure of this area, a WPOD wind measurement method is proposed. An anemometer based on this principle was mounted on a quadrotor UAV to build a wind measurement system. Compared with a standard anemometer, this system has satisfactory performance. Analysis of the resulting data indicates that the error of the system is ± 0.3 m/s and $\pm 2^\circ$ under hovering conditions and ± 0.7 m/s and $\pm 5^\circ$ under moving conditions. In summary, WPOD points to a new orientation for wind measurement under a small spatial–temporal scale.

Keywords: UAV; anemometer; wind measurement



Citation: Hou, T.; Xing, H.; Gu, W.; Liang, X.; Li, H.; Zhang, H. Wind Pressure Orthogonal Decomposition Anemometer: A Wind Measurement Device for Multi-Rotor UAVs. *Drones* **2023**, *7*, 366. <https://doi.org/10.3390/drones7060366>

Academic Editor: Diego González-Aguilero

Received: 3 April 2023
Revised: 24 May 2023
Accepted: 25 May 2023
Published: 31 May 2023



Copyright: © 2023 by the authors. Licensee MDPI, Basel, Switzerland. This article is an open access article distributed under the terms and conditions of the Creative Commons Attribution (CC BY) license (<https://creativecommons.org/licenses/by/4.0/>).

1. Introduction

The atmospheric boundary layer (ABL) is the lowest layer of the Earth's atmospheric structure. The ABL acts as an important bridge between the Earth's surface and the free atmosphere and is the leading site for all life activities. In recent years, with the increasing attention paid to the atmospheric environment [1], more and more experts point to the necessary development of high space-time resolution systems for detecting ABL. In particular, monitoring wind speed and direction is extremely important, as they visually characterize the state of the ABL. It is an essential reference for the study of atmospheric circulation, numerical weather prediction, ecological protection, and low-altitude aviation safety.

However, despite the need for such data, these measurements are not necessarily easy to acquire. Existing wind measurement equipment and methods generally lack the capability to perform high temporal and spatial resolution wind measurements at ABL. Several commonly available wind measurement devices and their application scenarios are shown in Figure 1.

(1) Ground-based weather stations and wind towers are the most commonly used near-surface (0–100 m) wind measurement equipment [2,3]. They have high wind measurement accuracy and satisfactory time resolution. Their spatial resolution is limited due to their fixed installation and high deployment costs [4].

(2) Sounding balloons and meteorological aircraft are often used for high-altitude (1–10 km) wind measurement [5]. These types of equipment use GPS or attitude sensors to establish a link between the wind and the flight state and to invert the wind speed and direction [6–11]. They are usually not very accurate and have an uncontrollable wind path [12–15].

(3) Doppler radar has been a popular piece of wind measurement equipment in recent years. It can be divided into L-band radar, S-band radar, and LIDAR in terms of the wavelengths of the electromagnetic waves emitted. It solves real-time wind velocity and direction by measuring the Doppler shift generated by the echoes of particles moving at different speeds in the atmosphere. Depending on the type of Doppler radar, it can extend from a few tens of meters to tens of kilometers or even further. It also has excellent time continuity and can generally achieve second-level responses. Doppler radar is a kind of wind measurement equipment with a wide area and high time resolution [16–19]. However, it has a limited spatial resolution. LIDAR, for example, generally only reaches a spatial resolution of 1–3 m. With very high deployment costs, Doppler radar has certain shortcomings in terms of refinement and large-scale deployment that are not suitable for the detection of ABL.

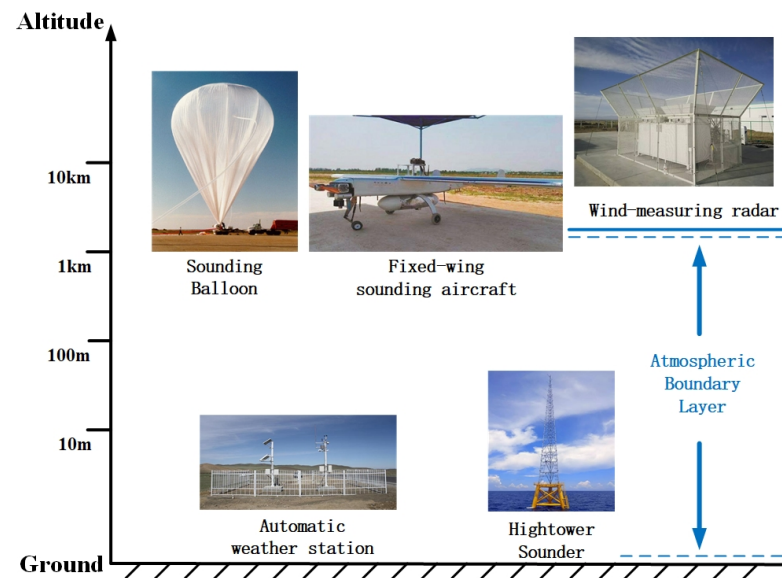


Figure 1. Wind measuring equipment for different altitudes.

The average thickness of the ABL is about 1–2 km (10–20% of the bottom of the troposphere) [20]. As mentioned above, there is a lack of suitable equipment to achieve high temporal and spatial resolution wind speed and direction detection in this interval. Fortunately, in recent years, coupling flight control systems and small aircraft have been extensively developed. Multi-rotor UAVs derived from this have become a potential platform for carrying wind measurement equipment. Considering the fast maneuverability of multi-rotor UAVs, which allow for fixed speed cruise and fixed point hovering, they are ideally suited to be used for detecting meteorological elements in the ABL [21]. It can carry wind measurement devices, thus enabling continuous measurement of wind velocity and direction at various spatial and temporal scales.

In approaches of access to relevant parameters, wind measurement methods based on multi-rotor UAV platforms can be divided into indirect measurement and direct measurement methods (IMM and DMM).

For IMM, Gonzalez points out that UAV flight regimes differ in different wind fields, and by building a mathematical model between the flight attitude and the wind field, it is possible to invert the wind speed and direction from its flight parameters [22]. He built three models to obtain wind speeds from the output of the UAV motors, the attack, roll, and pitch

angles of the airframe. With the rapid development of various non-linear models, artificial intelligence and machine learning techniques have been used in wind measurement models in recent years [23,24]. They are effective in improving the measurement performance of IMM. The advantage of the IMM method is that it does not require additional wind sensors to be deployed on the UAV platform. It reduces the UAV's take-off weight and increases its maneuverability. However, the IMM algorithm requires calculating the drag force of the multi-rotor UAV in the incoming flow. Before designing the algorithm, an accurate UAV drag coefficient must be obtained. At the same time, IMM will generate a massive amount of computing, which places higher demands on the control system of the UAV. It leads to poor portability of the indirect method of wind measurement and prevents its large-scale application in practical wind measurement scenarios.

DMM means that the wind parameters are obtained directly by mounted anemometers while the UAV is in flight. Riddell first measures wind velocity by attaching a wind cup to the UAV [25]. Wolf and Abichandani point out that rotor airflow was the primary factor affecting the accuracy of the measurements [26,27]. Ultrasonic anemometers installed on multi-rotor UAVs are currently the most chosen option for the DMM. Mallon designs a system with two A-type ultrasonic anemometers suspended underneath a quadrotor UAV [28]. Experiments prove that the system can be used for drawing wind profiles. However, he ignores the rotor airflow interference with the anemometer, which causes a significant impact on the accuracy of the wind measurement. Thorpe achieves three-dimensional detection of wind profiles from 0–50 m/s by installing an ultrasonic anemometer on a large eight-rotor UAV [29]. The results show that the anemometer is also subject to interference from the rotor airflow.

To overcome this problem, several scholars attempted to increase the mounting height of the wind sensor to keep it away from the rotor airflow. Wolf mounted a hot-wire anemometer 70 cm above a quadrotor UAV [26]. In a windless environment, the rotor airflow would interfere with the anemometer by about 0.5 m/s. Palomaki set up an ultrasonic anemometer 30 cm above a six-rotor UAV [30]. He compared this system with three ultrasonic wind measurement towers in various incoming flows. The results determined that its wind velocity error was between 0.3 and 0.8 m/s and its wind direction error was between 25° and 56°.

The wind measurement accuracy of DMMs is limited by the degree of coupling between the algorithm of the wind measurement sensor and the flight attitude of the UAV. Through comparative wind tunnel experiments, Li points out that ultrasonic anemometry produces more significant errors when tilting the UAV [31]. It is important to consider the effect of the attitude of the airframe on the wind measurement [32]. Geoffrey designed two wind measurement systems [33]. One was based on the DMM, with a Young Model 81000 ultrasonic wind gauge installed 520 mm above a six-rotor UAV. The other system was based on the IMM, a quadrotor UAV equipped with a rigid body model. The results showed that the DMM was significantly less accurate than the IMM wind measurement.

However, because DMMs are easier to develop and use, they have been widely used in meteorological and industrial detection. The reason for the poor accuracy of the DMM is that it requires ample installation space due to the size of the sensor. Therefore, the sensors are limited to the upper part of the multi-rotor UAV. However, if the sensor is not installed high enough to keep it away from the rotor airflow, the interference remains. Furthermore, if the sensor is installed too high, not only does it change the UAV's center of gravity, but the wind resistance moment generated by the sensor surface also affects the stability of the UAV. This phenomenon may even cause secondary interference to the wind measurement [34].

In order to improve the wind measurement accuracy of DMM quadrotor UAVs, we found a WTZ by analyzing the flow field of a quadrotor UAV. With respect to the spatial structure of this region, this paper first presents a wind measurement method based on the WPOD and develops a wind measurement sensor. Installing the sensor in the WTZ

weakens the rotor turbulence to ensure wind measurement accuracy. Therefore, the main contributions of this paper are as follows.

(1) A quadrotor UAV was accurately modeled. Computational fluid dynamics (CFD) software simulates the model's flowfield in various incoming flows. Based on the results, the intensity of the disturbing wind field in different areas around the quadrotor UAV was compared and analyzed. We found that there is a relatively static wind zone on the outside of the UAV blade, where the wind measurement sensor can not only improve the wind measurement accuracy. It also helps to reduce the wind resistance moment of the sensor, which can improve the flight stability of the multi-rotor UAV wind measurement system.

(2) We proposed the WPOD algorithm for the spatial characteristics of the relatively static wind region. The algorithm decomposes the wind pressure vector around the multi-rotor UAV, and the inverse performs the real-time wind velocity and direction based on Bernoulli's equation. At the same time, the algorithm creates a six-degree-of-freedom correction matrix based on the flight attitude of the UAV. The compensation of the variation of the wind pressure in each direction between the airframe coordinate system (ACS) and the geographical coordinate system (GCS) can be realized.

(3) We designed a wind measurement sensor based on the proposed theory and built a wind measurement system based on a high-lift quadrotor UAV. We carried out long wind measurement experiments with the UAV in hovering and moving conditions and showed that the system has satisfactory wind measurement results when compared with standard data from weather stations.

The rest of the paper is organized as follows. In Section 2, we analyze the flow field of a quadrotor UAV flying in various environments by CFD software and find a WTZ for installing wind sensors. In Section 3, the WPOD wind measurement method is proposed based on the structure of the WTZ, obtaining wind velocity and direction from wind pressure. In Section 4, we design an anemometer based on the WPOD principle and correct its pressure coefficient. In Section 5, the performance of the WPOD anemometer is verified by a comparison with a standard anemometer. In the final section, the work of the paper is summarized, the prospects for applying the WPOD wind measurement method are discussed, and the next steps in the research are outlined.

2. Flow Field Analysis of Quadrotor UAV

In this section, a quadrotor UAV of a common size is used as the object of study. Using CFD software simulates the UAV's flight flow field in various environments and analyzes the distribution of turbulence around the UAV.

2.1. Experimental Setup for Wind Field Analysis

Figure 2a shows the quadrotor UAV in the experiment. Its structural parameters are shown in Table 1.

Table 1. Key parameters of the quadrotor UAV simulation model.

	Parameters	Annotation
Blade	9045	Blade diameter 9 inches, pitch 4.5 inches.
Wheelbase	450 mm	Distance between two opposite motor shafts.
Spacing ratio	1.4	The ratio of the distance between the centers of two adjacent blades to the diameter of the single blade.

In order to simulate the UAV flight flow field to the maximum extent possible, the blade dimensions, wheelbase, and spacing ratio of the UAV model were strictly built. We simplified the fuselage structure to reduce the model complexity with a $100 \times 100 \times 30$ mm rounded-corners cube. The rotor arm was a rigid cylinder with a diameter of 1 cm. Figure 2b shows the quadrotor UAV model.

As shown in Figure 3, the static fluid domain of the experiment is a $10 \times 4 \times 4$ m cubic space, where the air density is 1.225 kg/m^3 , and the gravitational acceleration is 9.86 m/s^2 . We divided the space around the four rotors into separate dynamic domains. The center coordinates of rotors 1, 2, 3, and 4 were (3682, 1682, 0 mm), (4318, 1682, 0 mm), (4318, 2318, 0 mm), and (3682, 2318, 0 mm). Among them, rotor 1 and rotor 3 rotate clockwise, and rotor 2 and rotor 4 rotate counterclockwise. The UAV was positioned 6 m from the airflow inlet and 2.5 m from the ground, and X_B pointed to the airflow inlet.

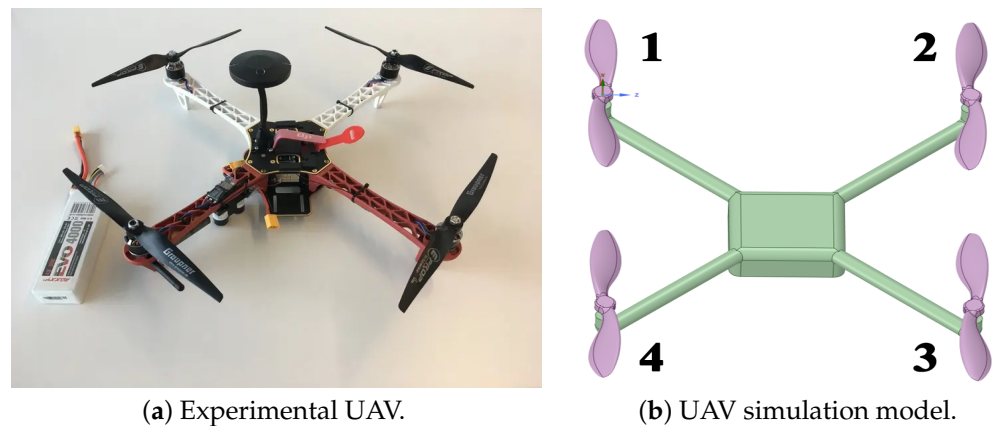


Figure 2. Experimental UAV and its simulation model.

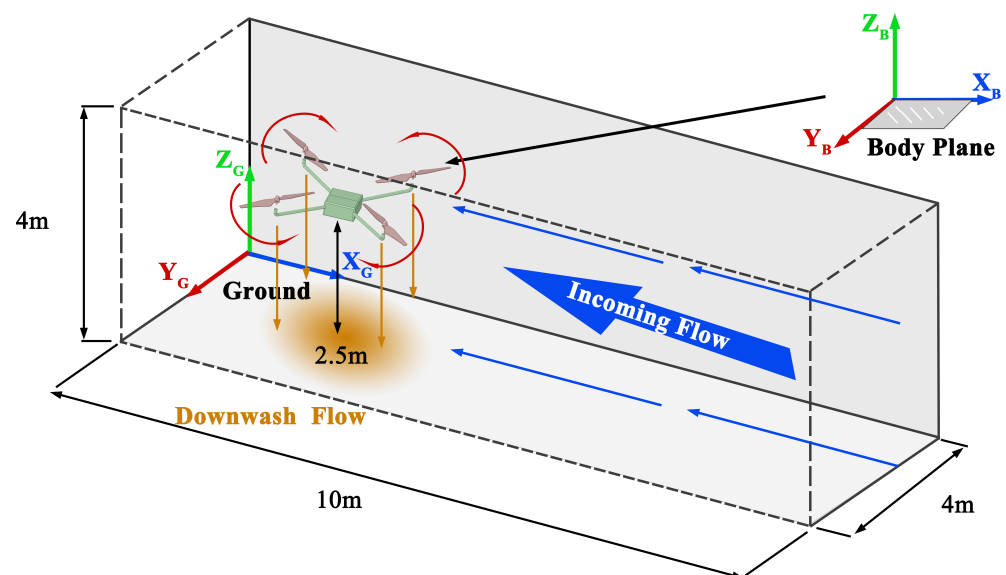


Figure 3. Simulated scenarios.

We completed the meshing of the computational domain in Ansys meshing, as shown in Figure 4. The total number of meshes was 5.0 million, and the quality values of the generated mesh structure achieved a maximum skewness of 0.68, minimum element quality of 0.36 and minimum orthogonal quality of 0.34.

Ansys Fluent was used for numerical simulation of the flow field. Because the rotor airflow is caused by rotating at high speed, the SST $K - \omega$ turbulence model was selected, which was suitable for complex shear stress flow [35]. This model combines the traditional $K - \epsilon$ and $K - \omega$ models in a weighted-average manner to provide a good balance between the simulation of the viscous sublayer and the near-wall flow. The pressure outlet boundary was used for the wall, and the inlet was set as velocity inlet; the upper surface of the total calculation domain and the lower surface were set as the non-slip wall. The sliding grid controls the moving field's rotation, and the rotation speed was set to 8000 rpm.

An unsteady transient calculation was adopted with a time step length of 0.001 s and 20 iterations for each step length. The convergence residual was set as 10^{-4} , and the flow field of the rotor after 10 s was calculated.

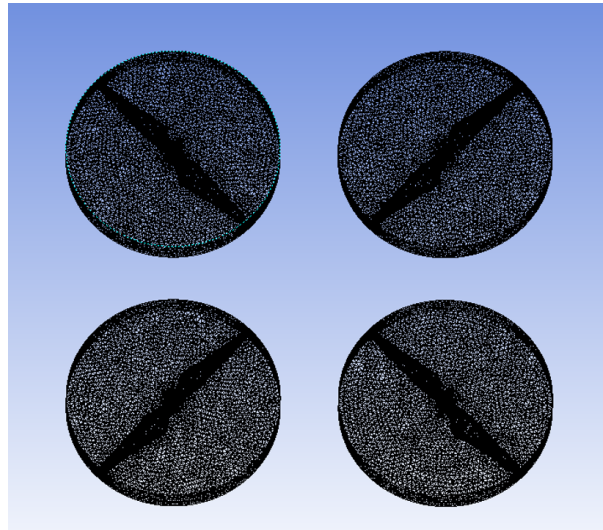


Figure 4. Meshing of blade dynamic domain.

2.2. Flow Field Analysis of the Quadrotor UAV Flight

There are two WTZs above and below the UAV in zones A and B of Figure 5. The black lines in Figure 5 show the sampling paths of the airflow velocity in these areas. The airflow intensities and locations discussed next are sampled from these lines. They are located in the center of the area, and all start at 0 mm from the UAV housing. Referring to Figure 6, the turbulence around the UAV body in zone A is quite low (0.04 m/s). As the altitude rises, the turbulence in zone A becomes more intense (reaching a maximum of 1.68 m/s at 164 mm). The intensity of the turbulence then gradually decreases. Zone B, a bell-shaped compartment with a diameter similar to the UAV fuselage and a height of nearly 40 cm, has the largest space for weak turbulence. In zone B, the turbulence velocity remains below 0.3 m/s along the Z-axis from the lower surface of the UAV. It increases significantly to a maximum of 12.3 m/s when zone B extends to the diffuse downwash flow.

The above simulation results agree with the experimental results of Wang [36]. For this reason, most wind sensors in active service are installed above or below the fuselage. At the same time, there is also a WTZ (zone C) outside the rotor in Figure 5a. Zone C starts at the end of the rotor arm. Although the first 10 cm of this zone is completely exposed within the strong downwash flow (wind velocities may reach 40 m/s), once it escapes from the downwash, the turbulence intensity will decrease significantly. At 230 mm from the rotor arm, the intensity starts to fall below zone B's, and at 500 mm from the boom, the velocity is just 0.2 m/s.

While the UAV is in a dynamic flow field, significant variation occurs in the flow field in zones A and B. Initially, the WD is the main disturbance generator, with the highest disturbance velocity near the fuselage. As it moves away from the fuselage, the power of the WD decreases, causing the velocity of the disturbance to decay rapidly. However, during the subsequent period, the WD and inhaled flow (IF) alternate in controlling the airflow movement in the region. This makes the turbulence extremely unstable in this zone, with large fluctuations. In zone A, after 100 mm from the fuselage, the IF becomes the dominant factor in the disturbance, and the disturbance velocity starts to decrease monotonically from 1.0 to 2.0 m/s. In zone B, due to the influence of the downwash airflow being blown away by the incoming flow, a peak in spoiler velocity still occurs after 200 mm from the fuselage and then gradually decreases.

The downwash airflow is the primary cause of disturbance in zone C. For the first 120 mm, the velocity of the disturbed flow is nearly the same as that of the downwash.

Because the downwash flow has a strong directional influence, the disturbance in zone C will quickly decrease once it is released from the downwash’s control.

Figure 7 shows the lowest turbulence interval in these zones for various incoming flows. It is clear that although zone A is by far the most common location for the anemometer to deploy, it is not an optimal choice. The space in zone A is so small that it is no more than 50 mm high in almost all scenarios. At the same time, it is precarious against turbulence, and consequently, it is difficult for wind sensors to avoid turbulence effectively here.

On the whole, zone B provides better anti-disturbance in spaces up to 200 mm from the body. However, as Zone B is directly below the UAV, we must take into account the height of the landing gear (typically only 50–150 mm), and this space is too small for the size of the anemometer. Furthermore, the turbulence in zone B fluctuates significantly with the distance from the UAV. The sensor deploying position needs to be further defined to avoid interference. Therefore, it can be concluded that installing wind measurement sensors in zone B is complex and a safety hazard.

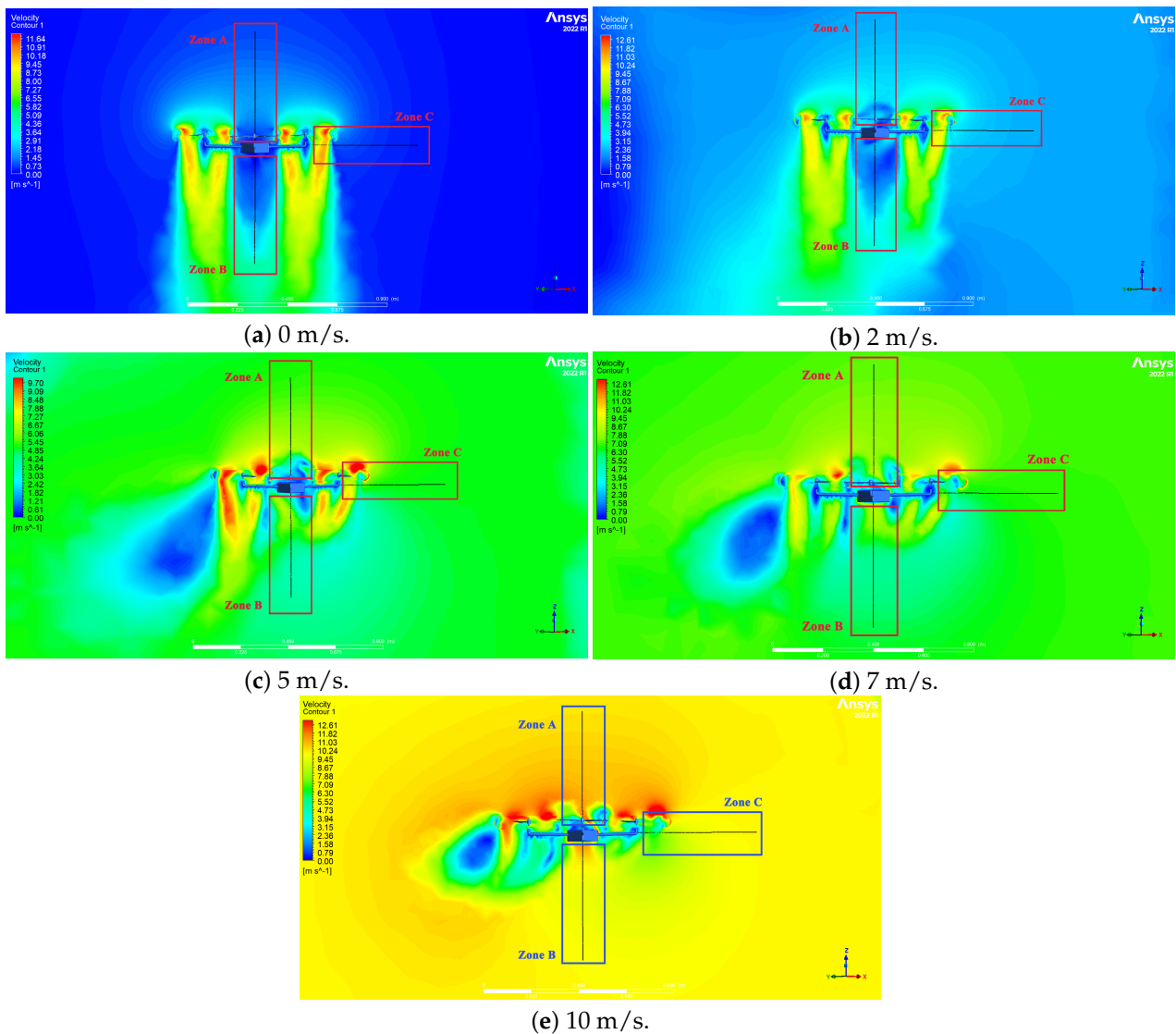


Figure 5. Velocity nephogram of the quadrotor UAV at different velocities of incoming flow.

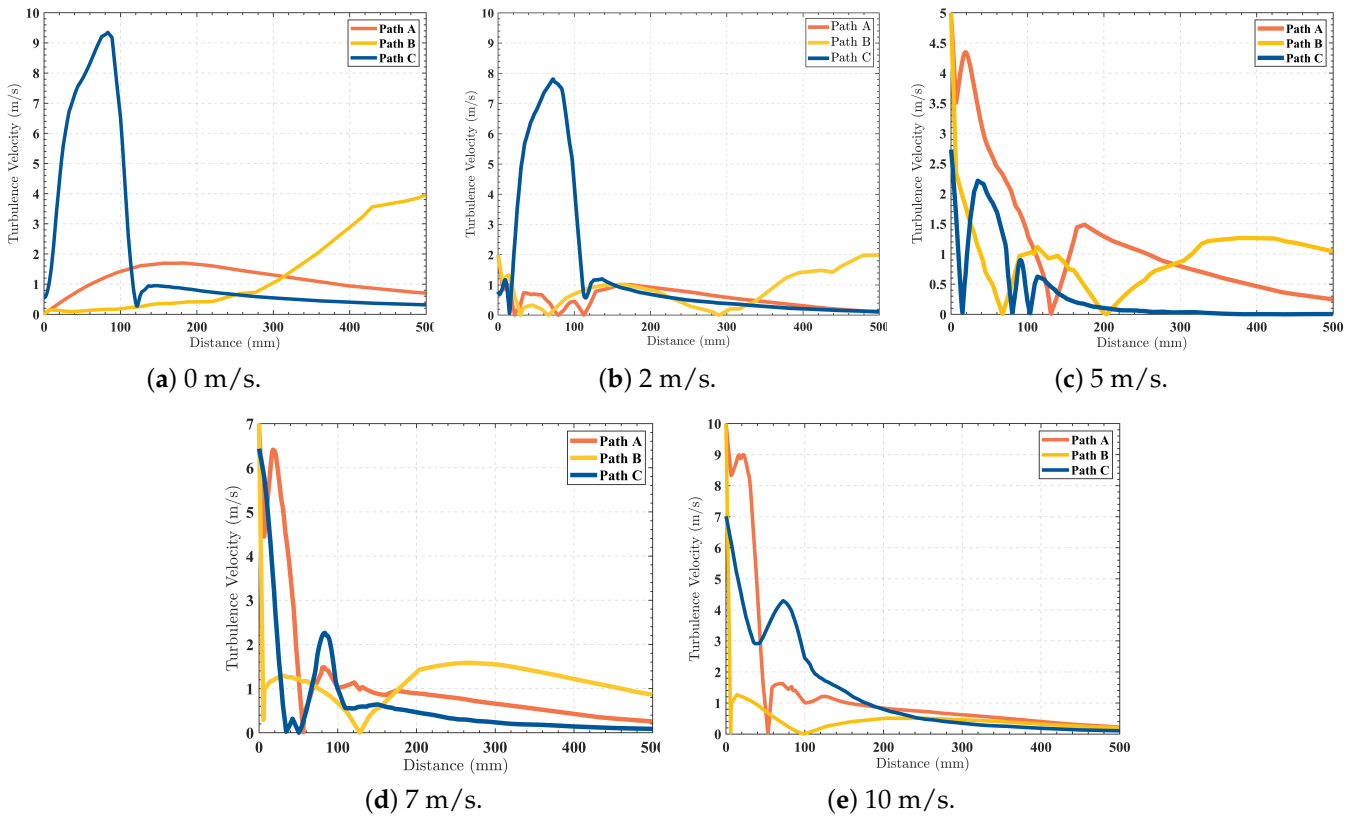


Figure 6. Disturbance intensity on different sampling paths.

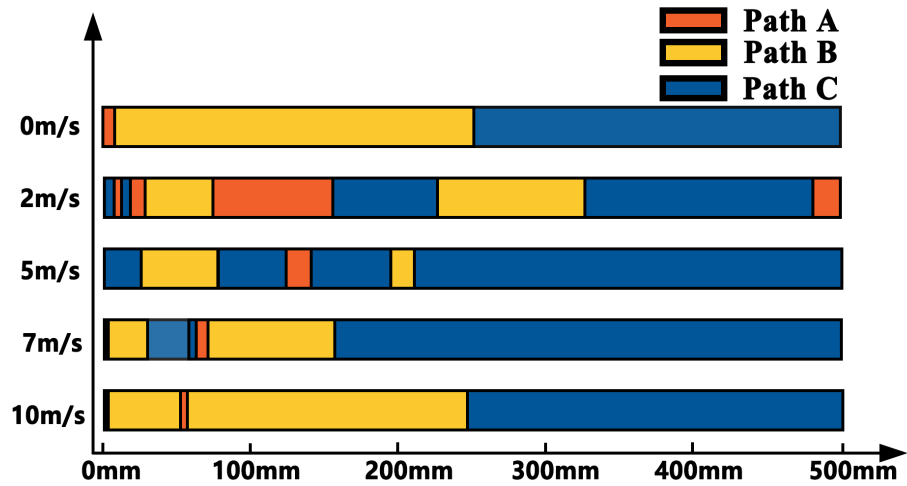


Figure 7. A, B and C with minimum disturbance in different incoming flow velocities.

Zone C shows a decent anti-turbulence performance. After a distance of 270 mm from the fuselage, the turbulence therein is kept to a minimum. Although zone C is not optimal in the 100–250 mm range, the internal disturbance velocities are below 1.0 m/s, which is the same order of magnitude as the optimal zone. In all scenarios, once freed from the initial downwash, the disturbance intensity of zone C remains relatively low. At the same time, the location of zone C avoids the landing path of the UAV, which leaves a larger space to install the wind sensor. Therefore, it is safe to assume that zone C is a more suitable location for wind sensors than others.

3. The Wind Pressure Orthogonal Decomposition Wind Measurement Method

As seen in Section 2, zone C is annular with a narrow inner and wide outer zone. Here the conventional ultrasonic and thermal anemometers are too large to be installed. In order to miniaturize the wind sensor, a WPOD wind measurement method was designed based on Bernoulli's equation.

3.1. Wind Measurement Principles

Assume that air is an incompressible gas. At this point, according to Bernoulli's equation: in an ideal flow field, the static pressure at the same height on the same flow line is equal everywhere, and the sum of its dynamic pressure is the total pressure [37], as shown in Equation (1).

$$P_{Dynamic} + P_{Static} = P_{Total} \quad (1)$$

where $P_{Dynamic}$ is the dynamic pressure somewhere on this flow line and is proportional to the square of the fluid velocity (as shown in Equation (2)), ρ is the fluid density, and v is the fluid velocity. P_{Static} is the static pressure on this flow line. As shown in Figure 8, there are two thin tubes with parallel flow lines and opposite opening directions in the flow field.

$$P_{Dynamic} = \frac{1}{2}\rho v^2 \quad (2)$$

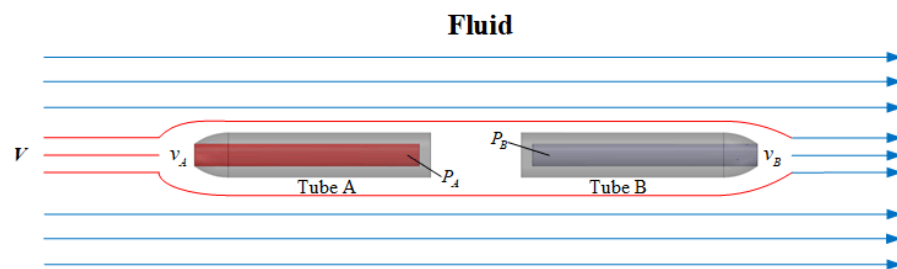


Figure 8. Wind measurement principle of Bernoulli's equation.

Since the opening of tube A is facing the incoming flow, the velocity of v_A is approximately equal to the incoming flow ($v_A = V$), and the internal pressure is the total pressure ($P_A = P_{Total}$). At this point, from Equations (1) and (2), the following relationship holds as $P_A = \frac{1}{2}\rho v_A^2 + P_{Static}$. The opening of tube B is completely back to the incoming flow, and v_B is almost completely static ($v_B = 0$ m/s). Therefore, the pressure inside tube B is consistent with the static pressure of the air at that line ($P_B = P_{Static}$). Furthermore, because the heights of point A and point B are the same, the flow velocity V can be solved by Equation (3).

$$V = v_A = \sqrt{\frac{2(P_A - P_B)}{\rho}} = \sqrt{\frac{2\Delta P}{\rho}} \quad (3)$$

In practical measurements, viscosity affects the state of motion of the air. It will cause $v \neq \sqrt{\frac{2\Delta P}{\rho}}$ to not be established strictly. A correction factor K needs to be introduced to correct the actual wind velocity, as shown in Equation (4).

$$v = K\sqrt{\frac{2\Delta P}{\rho}} \quad (4)$$

Based on this principle, as shown in Figure 9, four tubes are set orthogonal to each other in a two-dimensional plane. Combining orthogonal decomposition principles, they can measure the velocity and angle of the airflow from any direction in the plane.

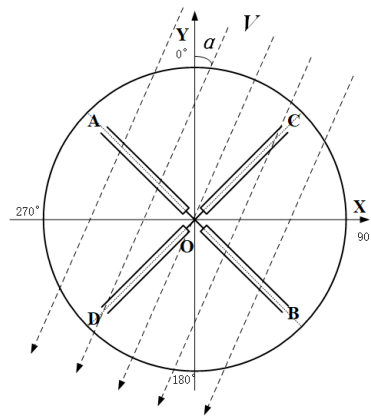


Figure 9. Wind measurement model based on Bernoulli’s equation in two dimensions.

Figure 9 represents the relationship between the two-dimensional wind measurement model and the incoming flow. The angle between tubes A, B, C, and D is 90°. Let the angle bisector between tube A and tube C be the Y-axis to establish a coordinate system. In this system, as shown by Equations (5)–(7), the vector sum of the airflow velocities in the AB and CD directions is the incoming velocities V .

$$V_{AB} = K\sqrt{\frac{2(P_A - P_B)}{\rho}} \tag{5}$$

$$V_{CD} = K\sqrt{\frac{2(P_C - P_D)}{\rho}} \tag{6}$$

$$V = \sqrt{V_{AB}^2 + V_{CD}^2} \tag{7}$$

Angle α between V and the Y-axis is shown in Equation (8).

$$\alpha = \left\{ \begin{array}{ll} \arctan\left(\frac{V_{CD}}{V_{AB}}\right) - 45^\circ, & V_{AB} > 0, V_{CD} > 0 \\ \arctan\left(\frac{V_{CD}}{V_{AB}}\right) + 45^\circ, & V_{AB} < 0, V_{CD} > 0 \\ \arctan\left(\frac{V_{CD}}{V_{AB}}\right) + 135^\circ, & V_{AB} < 0, V_{CD} < 0 \\ \arctan\left(\frac{V_{CD}}{V_{AB}}\right) + 225^\circ, & V_{AB} > 0, V_{CD} < 0 \\ 45^\circ, & V_{AB} = 0, V_{CD} > 0 \\ 135^\circ, & V_{AB} < 0, V_{CD} = 0 \\ 225^\circ, & V_{AB} = 0, V_{CD} < 0 \\ 315^\circ, & V_{AB} > 0, V_{CD} = 0 \end{array} \right. \tag{8}$$

3.2. Attitude—Wind Velocity Correction Algorithm

Assuming that the multi-rotor UAV is a rigid body, the wind velocity measured by the model in Section 3.1 is the speed of the UAV to the surrounding airflow. It is a vector sum of the natural wind velocity with the flight speed of the UAV, which can not truly reflect the natural wind velocity. At the same time, the coordinate system defined by the model is parallel to the plane of the UAV. The UAV will generate pitch and roll angles to maintain a stable attitude during flight. As a result, the wind velocity and direction measured by the model are only relative to the airframe coordinate system (ACS) of the UAV and deviate from the macroscopic geographical coordinate system (GCS). To determine the movement of the wind in the GCS, it is necessary to establish a kinematic equation and to correct the wind measurement model.

As shown in Figure 10, ACS ($Ox_B y_B z_B$) and GCS ($Ox_G y_G z_G$) are defined to describe the UAV attitude.

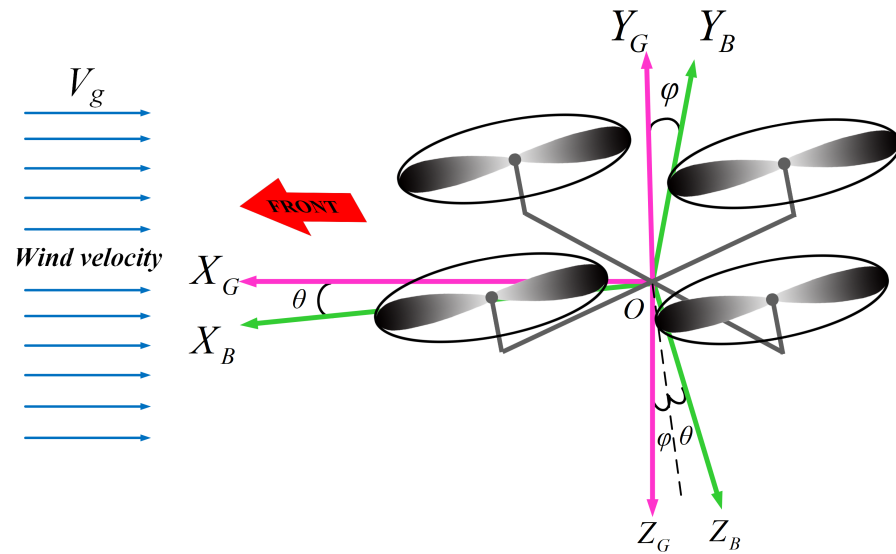


Figure 10. Relationship between the ACS and GCS.

Define the UAV’s barycenter as the origin O . In $OX_B Y_B Z_B$, the X_B direction is aligned with the axis of symmetry of the body. Vertical X_B in the UAV’s symmetry plane is the Z_B , and vertical Y_B in the $OX_B Z_B$ plane points to the right of the airframe. The Z_G axis lies in the airframe of the lead hammer and is perpendicular to X_G . X_G is the projection of X_B on an airframe parallel to the ground and past the O . Define the Z_G axis that lies in the airframe of the lead hammer and that is perpendicular to X_G . The pitch angle (θ) is the angle between the longitudinal axis of the airframe and the ground, which is between $X_G O$ and $X_B O Y_G$. Similarly, the angle between the horizontal axis and the ground is the roll angle (φ) and is represented in the coordinate system as the angle between $O Y_B$ and $X_G O Y_G$.

Usually, mapping of the free vector from the GCS to ACS can be accomplished by creating a rotation matrix R , whose expression is:

$$R(\Theta) = \begin{pmatrix} \cos \theta & 0 & \sin \theta \\ -\sin \theta \sin \varphi & \cos \varphi & \cos \theta \sin \varphi \\ -\sin \theta \cos \varphi & -\sin \varphi & \cos \theta \cos \varphi \end{pmatrix} \tag{9}$$

Since the inverse of the rotation matrix is its transpose, mapping of the velocity vector from $OX_B Y_B Z_B$ to $OX_G Y_G Z_G$ can be expressed as:

$$V_G = R(\Theta)^T V_B \tag{10}$$

Substituting Equations (5) and (6) into Equation (10) gives the projections of V_{AB} and V_{CD} in $OX_G Y_G Z_G$:

$$V_{G,AB} = R(\Theta)^T \begin{pmatrix} \cos(\frac{\pi}{4}) V_{B,AB} \\ -\sin(\frac{\pi}{4}) V_{B,AB} \\ 0 \end{pmatrix} = \frac{\sqrt{2}}{2} V_{B,AB} \begin{pmatrix} \cos \theta + \sin \theta \sin \varphi \\ -\cos \varphi \\ \sin \theta - \cos \theta \sin \varphi \end{pmatrix} \tag{11}$$

$$V_{G,CD} = R(\Theta)^T \begin{pmatrix} \cos(\frac{\pi}{4}) V_{B,CD} \\ \sin(\frac{\pi}{4}) V_{B,CD} \\ 0 \end{pmatrix} = \frac{\sqrt{2}}{2} V_{B,CD} \begin{pmatrix} \cos \theta - \sin \theta \sin \varphi \\ \cos \varphi \\ \sin \theta + \cos \theta \sin \varphi \end{pmatrix} \tag{12}$$

Assuming that the UAV flight speed is $V_{UAV} = (x \ y \ z)^T$, to avoid the sensor being affected by the UAV airspeed, the real wind (V_R) velocity needs to be calculated by subtracting the airspeed from the measured wind velocity. As shown in Equations (13) and (14):

$$V_{R,AB} = V_{G,AB} - V_{UAV} \tag{13}$$

$$V_{R,CD} = V_{G,CD} - V_{UAV} \tag{14}$$

In the above equations, V_R demonstrates the actual components of wind velocity in the GCS. In the meteorological detection field, we are generally more focused on the lateral velocity of the wind; the component of the wind velocity on the Z-axis can be ignored. At this point, the surface wind velocity V_w can be obtained by combining Equations (7), (13) and (14). As shown in Equation (15):

$$V_w = \begin{pmatrix} x_w \\ y_w \\ 0 \end{pmatrix} = V_{R,AB} + V_{R,CD} \tag{15}$$

Combining Equations (8) and (15) will obtain the angle between wind velocity and OX_G in $OX_GY_GZ_G$:

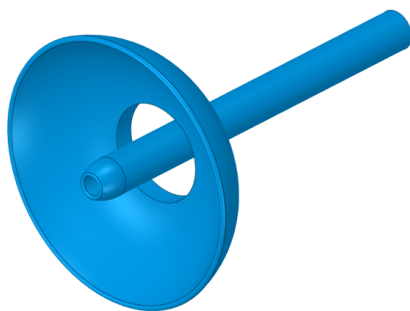
$$\alpha = \begin{cases} \arctan\left(\frac{y_w}{x_w}\right), & x_w > 0, y_w > 0 \\ \arctan\left(\frac{y_w}{x_w}\right) + 90^\circ, & x_w < 0, y_w > 0 \\ \arctan\left(\frac{y_w}{x_w}\right) + 180^\circ, & x_w < 0, y_w < 0 \\ \arctan\left(\frac{y_w}{x_w}\right) + 270^\circ, & x_w > 0, y_w < 0 \\ 0^\circ, & x_w > 0, y_w = 0 \\ 90^\circ, & x_w = 0, y_w > 0 \\ 180^\circ, & x_w < 0, y_w = 0 \\ 270^\circ, & x_w = 0, y_w < 0 \end{cases} \tag{16}$$

4. WPOD Anemometer

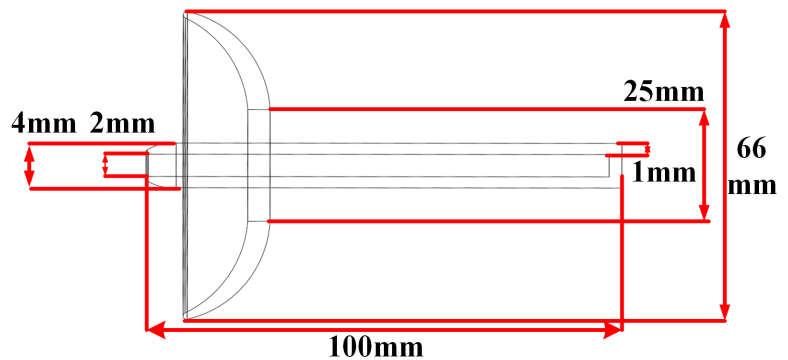
In this section, we design a novel anemometer based on the spatial structure of the WTZ (zone C) and the WPOD principle.

4.1. WPOD Anemometer Construction

This paper uses four rigid tubes of 100 mm length, 2 mm inner diameter, 4 mm outer diameter, and 1 mm wall thickness to capture wind pressure in the incoming flow, collectively referred to as the pressure-sensitive chamber (PSC). To further reduce the turbulence interference with the wind measurement, a hemispherical shell fairing with a diameter of 66 mm and a wall thickness of 2.5 mm is installed around the opening of the PSC. The bottom of the fairing has a 25 mm radius opening through which the PSC passes. This opening is used to reduce the wind resistance caused by the incoming flow being blocked by the fairing. We refer to the set of PSC and the fairing as the wind measurement unit (WMN), as shown in Figure 11.



(a) The wind measurement unit model.



(b) The measurement unit model detailed.

Figure 11. The measurement unit.

Four sets of WMUs are made from PLA by 3D printing and are mounted at 90° to each other around the quadrotor UAV, as shown in Figure 12. Based on the analysis of zone C in Section 2, we set the relationship between the WMUs and the UAV as follows: (1) the vertical distance between each WMU and the paddle is 55 mm; (2) the horizontal distance between the WMU and the UAV arm is 145 mm. Since the four WMS are deployed in an orthogonal arrangement, there must be one or two WMS units in the incoming flow during the UAV flight in any direction of the wind. In this case, using the WPOD model, the wind velocity and direction can be inverse performed from the wind pressure difference in the WMUs.

There are two SDP810 sensors that are used to measure the wind pressure difference. They receive the air pressure from PSCs through a set of silicone hoses. The SDP810 weighs 6 g, operates at 3.3 V, has a range of $-125\sim+125$ pa, can withstand a maximum pressure of 2 kpa, has a response time of less than 5 ms, and supports the IIC protocol to output data with a resolution of 16 bits to the main control unit (MCU). The WPOD model shows that the SDP810-based anemometer can provide a wind measurement range of $0\sim 20$ m/s, a wind measurement resolution of 0.07 m/s, and a maximum operating wind measurement speed of 57 m/s. These parameters are able to meet the requirements of wind measurement tasks in general environments.

We chose the STM32F103C8T6 as the MCU for the WPOD anemometer. It will drive the SPD810 to acquire the raw wind pressure data with a sampling frequency of 200 Hz. At the same time, the MCU will read the flight attitude from the UAV's flight control in real time through serial communication. Finally, it calculates the real-time wind velocity and direction and transmits the data back to the ground through a 2.4 GHz wireless transmission model.

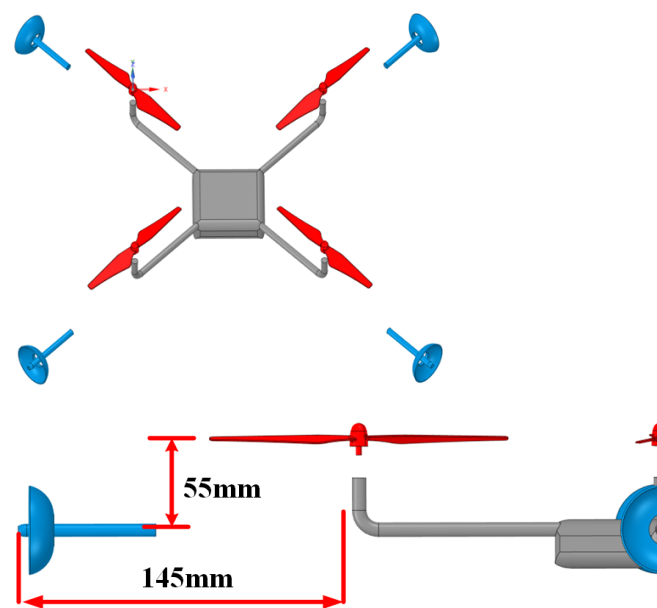


Figure 12. Position of the wind measurement unit in relation to the airframe.

4.2. WMU Performance Verification and Calibration

As seen from Section 3.1, K is an essential parameter in the WPOD method, which directly relates to wind measurement accuracy. We also use meshing and fluent on the Ansys platform to simulate and analyze the values of K . At this point, the total number of meshes is 2.2 million, the maximum skewness is 0.48, the minimum element quality is 0.42, and the minimum orthogonal quality is 0.38. The boundary conditions and turbulence model in the simulation are consistent with those in Section 2.

We measured the correction coefficients of WMUs by a set of validation experiments. Four WMUs were placed in a speed gradient field of $0\sim 10$ m/s at 15° intervals, and the

pressure changes inside the PSCs were measured as shown in Figure 13. The performance of the WPOD model was verified by inverting the prevailing wind velocity based on the pressure difference. The results are shown in Figure 14.

Figure 14 shows that when the wind direction is not 45°, the inversion results by WMU are linearly related to the standard wind velocities. In this way, we can determine the ratio of standard wind velocity to measured wind velocity as a constant, i.e., $K = 0.68$. Combined with Figure 13a–c, it can be considered that there is no evident correlation between K and the windward angle.

A special phenomenon occurs when the wind direction is 45°. Since the WMUs on the leeward side are in the wake turbulence of the windward side, the wind velocity around the leeward WMUs decreases sharply, and its internal static pressure increases, which leads to a significant change in the slope of the 45°, at which $K = 0.84$.

However, since the quadrotor UAV is a mobile platform, the deviation caused by this particular angle value can be ignored. When setting $K = 0.68$, there is a deviation of the measured wind velocity from the standard wind velocity at each windward angle, as shown in Table 2.

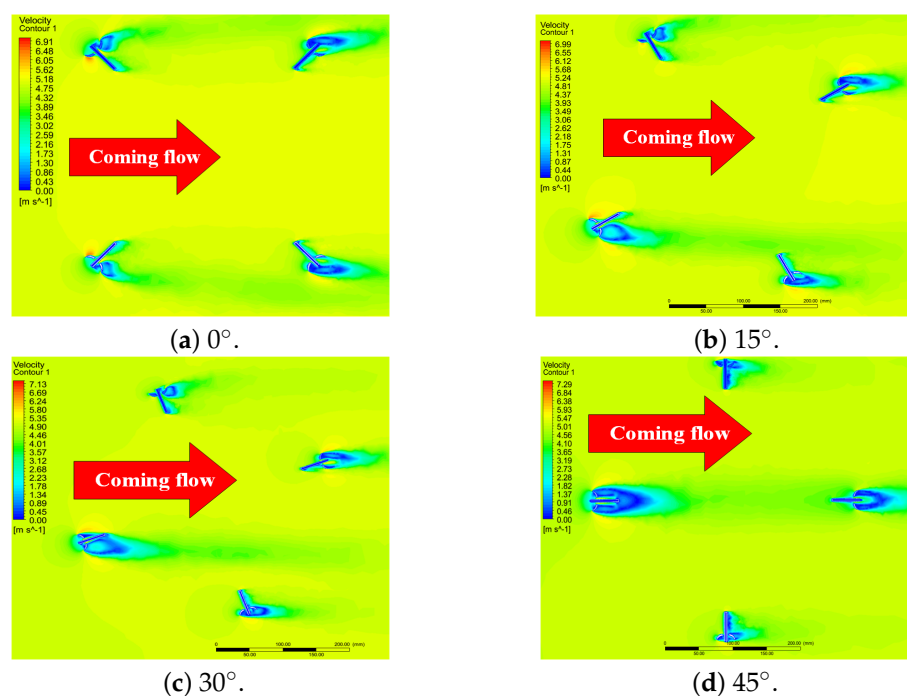


Figure 13. Velocity nephograms at different incidences of the WMU when the incoming velocity is 5 m/s.

Table 2. Wind velocity deviation of the WMUs.

	0°	15°	30°
RMSE	0.10	0.07	0.09
MAE	0.03	0.02	0.03
R^2	0.99	0.99	0.99

After correction, the measurement results for the WMUs are as follows: root mean squared error (RMSE) is less than 0.1 m/s, coefficient of determination (R^2) is 0.99, and the mean absolute error (MAE) is less than 0.03 m/s. Therefore, this experiment proves that the measured values of WMUs based on WPOD theory have a minimal deviation from the standard, and K is able to correct its wind measurement results effectively.

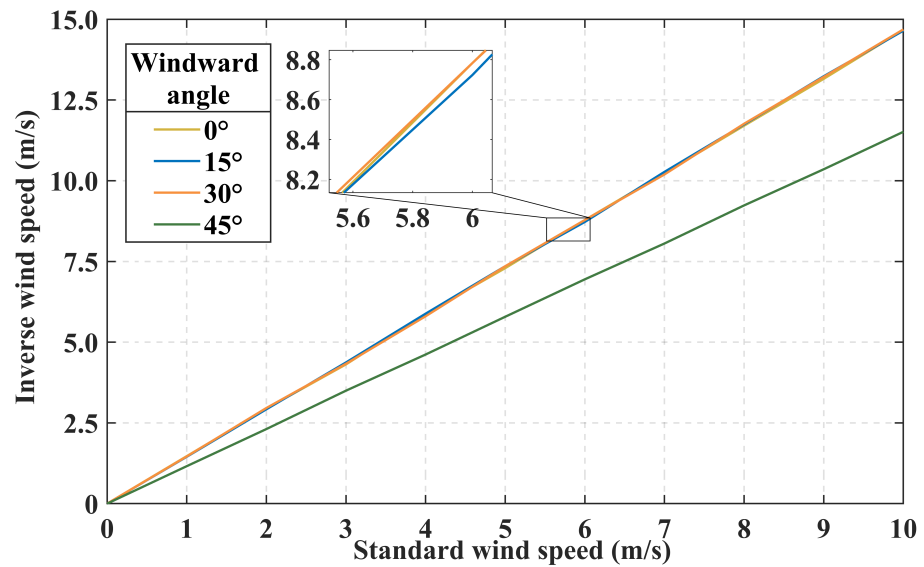


Figure 14. Relationship between incoming flow velocity and inversion velocity in different states.

5. Field Experiment and Analysis

We developed two sets of experiments based on the flight status of the UAV: wind measurement experiments while the UAV is hovering and while it is moving. They were conducted at 12:00 on 26 January 2021 and at 19:00 on 27 January 2021. In the experiment, standard data were measured by a wind cup fixed at 10 m from the ground. The indicators of the wind cup are as follows: 1200 Hz sampling frequency, measurement span 0–50 m/s and 0–359°, and accuracy of ±0.03 m/s and ±1.5°. The experimental site was Nanjing University of Information Technology Jiangsu (32°12′20.41″ N, 118°42′18.29″ E, average altitude 22 m).

A high-lift quadcopter UAV platform was built to carry the WPOD anemometry system, with the detailed configuration shown in Table 3. The complete wind measurement system is shown in Figure 15.

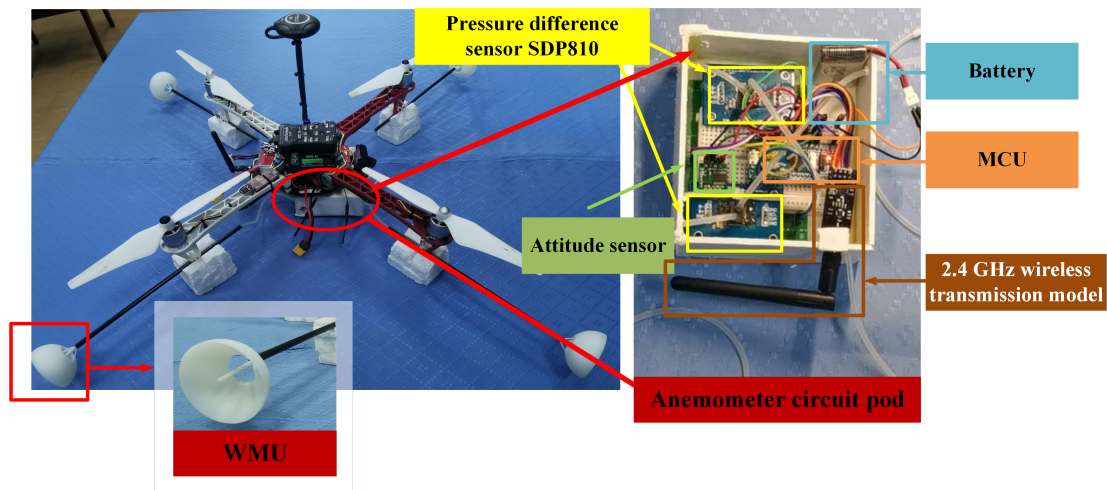


Figure 15. WPOD anemometry system and its various components.

Table 3. Parameters of the quadcopter UAV.

Category	Frame	Control System	Blade	Electronic Speed Controller	Motor
Parameters	DJI F450	Pixhawk 2.8.4	9450 Blade*4	X-rotor 20A *4	DIJ 2312S Brushless motor

5.1. Hovering Wind Measurement Experiment

The UAV hovered at a height of 10 m, 35 m from the wind cup (yellow dot in Figure 16). After the UAV's flight status stabilized, the system returned wind velocity and direction data. The results of the comparison with the wind cup are shown in Figure 17.

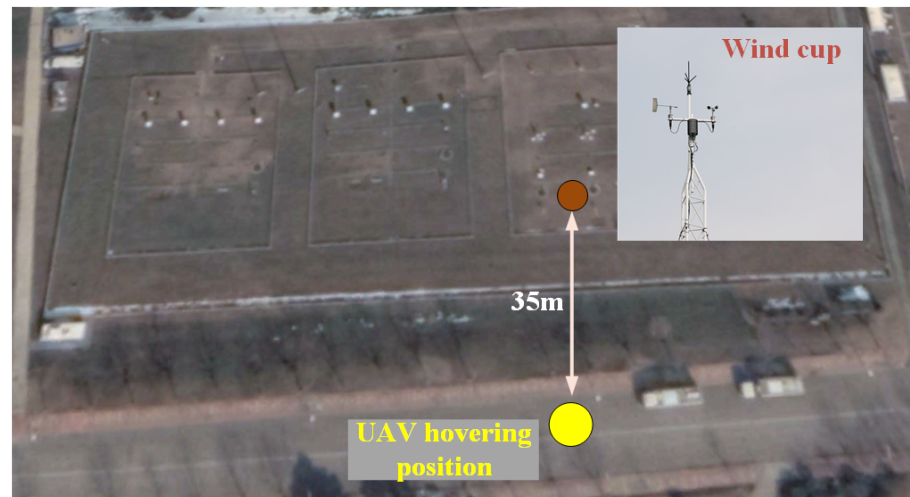
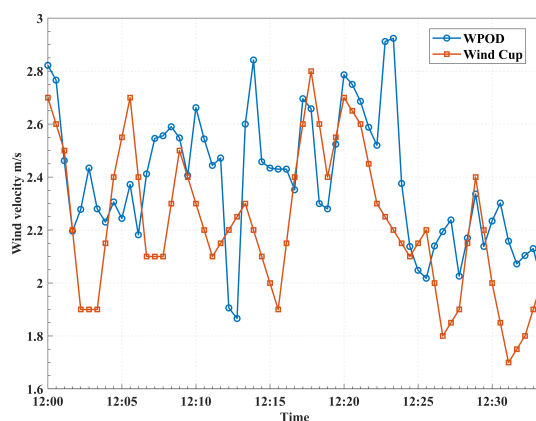
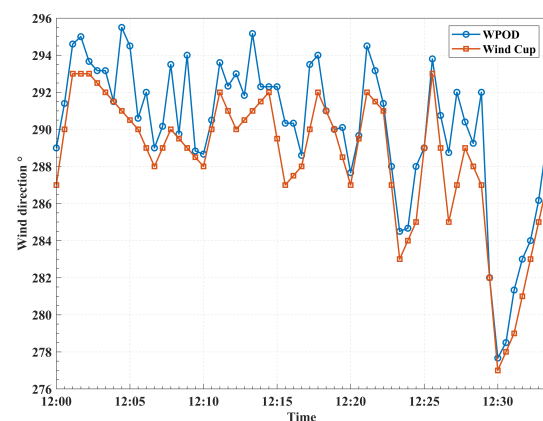


Figure 16. Hovering wind measurement experiment scenario.

Figure 17a demonstrates that the wind velocity values measured by the system are generally higher than the wind cup, with an MAE of 0.26 m/s and RMSE of 0.31 m/s. The wind velocity error was less than 0.3 m/s at over 91.8% of the sampling points.



(a) Wind velocity measurement results.



(b) Wind direction measurement results.

Figure 17. Wind measurement results of the system in hovering condition.

In the experiment, the hovering UAV would drift at 2–3 m per minute, perhaps induced by insufficient GPS positioning accuracy. We performed manual position correction at 12:06:00, 12:14:00, and 12:23:00 to prevent the UAV from drifting too far or from colliding with other obstacles. The UAV's flight speed sudden changes may have contributed to the significant measurement error at these moments. At 12:14:00, the UAV had a low battery alarm and was then landed and to replace the battery. The system did not update the anomaly data during the landing and take-off to facilitate data processing.

Figure 17b shows the wind direction measurement results of the WPOD anemometry system. It had an MAE of 1.73° and RMSE of 2.20°. Apart from the few anomalies analyzed above, the direction error remained below 2°.

5.2. Moving Wind Measurement Experiment

In the moving wind measurement experiment, we controlled the quadrotor UAV through the UAV ground station (Mission Planner) to travel in a 60×20 m rectangular path at a speed of 2 m/s. It is shown in Figure 18.

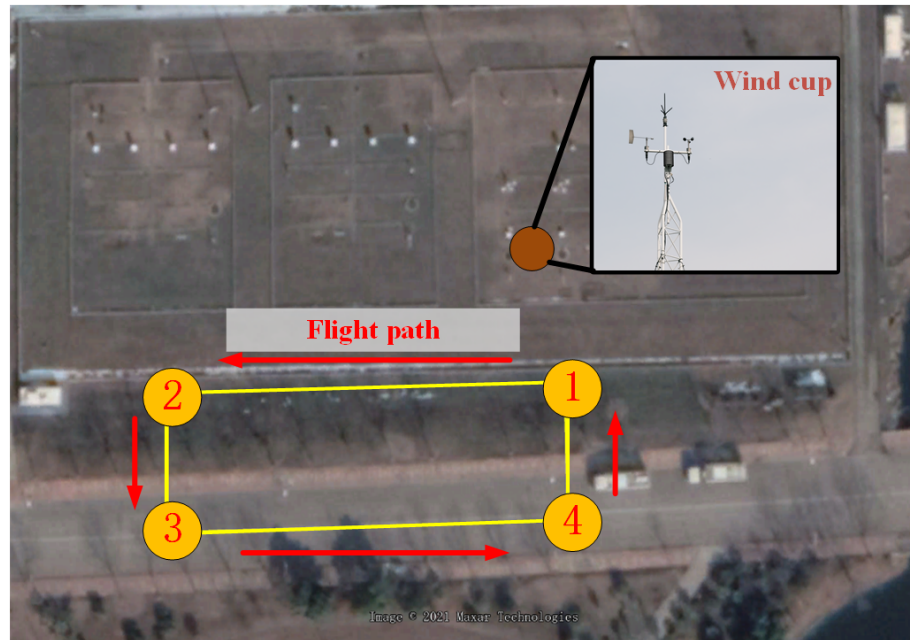
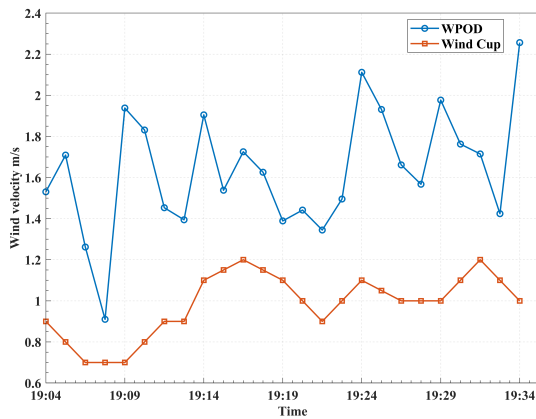
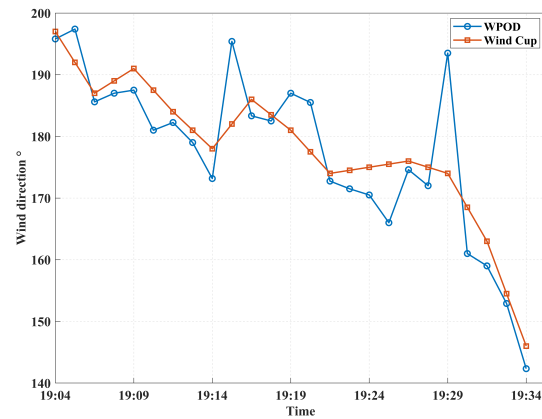


Figure 18. Moving wind measurement experiment scenario.

As shown in Figure 19, the accuracy of the WPOD anemometer is significantly lower in the traveling state than during hovering, with an MAE of 0.68 m/s and RMSE of 0.73 m/s.



(a) Wind velocity measurement results.



(b) Wind direction measurement results.

Figure 19. Wind measurement results of the system in moving condition.

In Figure 18, ①, ②, ③, and ④ are the corners of the rectangular path. The UAV speed should have reduced to 0 m/s and turned 90° when it reached these four corners. However, during the trial, the UAV was unable to halt directly and precisely at the inflection point due to the limitations of GPS or flight control positioning accuracy. The UAV performed a series of maneuvers to finish the turning procedure. This caused drastic changes in the pressure and attitude of the WPOD anemometry system, which hurt the wind measurement. Meanwhile, during the steering of the UAV around the Z_B axis, centrifugal force can change the pressure inside the pressure-sensitive chamber, which also causes measurement errors. In Figure 19a, the sudden increase in wind speed at 19:04:30, 19:06:00 p.m., 19:06:30, 19:08:00,

19:12:00, 19:12:30, and 19:16:00 should all be caused by UAV steering. Excluding these steering points, the absolute wind speed error remained within 0.7 m/s. The MAE of the wind angle measured by the WPOD anemometry system was 4.9° , the RMSE was 6.5° , and the correlation coefficient was 0.89. Figure 19b also shows that the angle's absolute error was less than 5° , except for the outliers located at the four inflection points. Considering that the experimental platform was in motion, these results are satisfactory overall.

6. Discussion

In this study, we proposed a WPOD wind measurement method for multi-rotor UAVs. We analyzed the flow field of a quadrotor UAV and identified a WTZ. Mounting the wind sensor will effectively circumvent the rotor turbulence. We designed an orthogonal structure of the wind meter based on the WPOD principle and corrected its pressure coefficient. We compared the performance of the WPOD anemometer with a standard anemometer in hovering and moving conditions.

Our results indicate that the RMSE of the system is 0.31 m/s and 2.2° under hovering conditions and 0.73 m/s and 6.5° under moving conditions; the MAE of the system is 0.26 m/s and 1.73° under hovering conditions and 0.68 m/s and 4.9° under moving conditions. Compared with the existing quadrotor UAV wind measurement equipment (as shown in the Table 4), the results are satisfactory.

Table 4. Comparison with existing quadrotor UAV wind measurement equipment.

Wind Sensor	Accuracy (RMSE)	
	Speed (m/s)	Direction ($^\circ$)
DS-2 2D ultrasonic anemometer [30]	0.27–0.67 m/s Under wind speed 1–5 m/s.	25° – 56° Under wind speed 1–5 m/s.
Tri-Sonica Mini 2D ultrasonic anemometer [26]	1.13 m/s Under wind speed 6.75 m/s.	133.36° Under wind speed 6.75 m/s.
FT702 2D ultrasonic anemometer [33]	0.6 m/s Under wind speed 11.0 m/s.	12.0° Under wind speed 11.0 m/s.
Young Model 81000 ultrasonic anemometer [33]	1.85 m/s	113.67°
Tri-Sonica Mini [33]	1.08 m/s	87.05°
WPOD (this article)	0.31 m/s in hovering position 0.73 m/s in moving position	2.20° in hovering position 6.50° in moving position

These findings demonstrate that the WPOD method is a novel and effective way to measure wind under a small spatial-temporal scale. It can overcome some of the limitations of existing methods, such as large sensor size, high installation complexity, low spatial resolution, and high deployment cost. The WPOD anemometer can be used as a platform for carrying wind measurement devices on multi-rotor UAVs, which can improve the spatial and temporal resolution of wind measurement in the ABL.

However, there are some limitations of this study that need to be addressed. First, we only tested the WPOD anemometer on a quadrotor UAV with a specific size and configuration. The applicability of this method to other types of multi-rotor UAVs or different environmental conditions remains to be verified. Second, the anemometer performance is heavily reliant on the UAV's steady flying. The performance of the WPOD anemometer in complex scenarios may be affected by factors such as airflow separation, turbulence intensity, or ground effect. Third, as the WPOD theory is based on a 2D plane, it may not be possible to effectively measure the wind speed and direction in the vertical direction.

7. Conclusions

This article proposes a WPOD anemometer to achieve accurate wind measurement on a quadrotor UAV platform. Based on CFD, we found a WTZ around the UAV, which is more suitable for mounting wind measurement devices. Then, the WPOD model was proposed to allow for wind measurement in the special shape of the WTZ. The method was based on Bernoulli's equation, which can invert the wind speed and direction from the wind pressure around the UAV. Finally, we designed a WPOD anemometry system and verified its performance through two comparison experiments. When the UAV was hovering, the wind velocity error was ± 0.3 m/s, and the direction error was $\pm 2^\circ$; with the UAV moving, the velocity error was ± 0.7 m/s, and the direction error was $\pm 5^\circ$.

The combination of anemometers and multi-rotor UAVs can compensate for the current blind spot in wind measurement at low altitudes, which will effectively improve the spatial and temporal resolution of wind measurements. This paper presented a wind measurement strategy for multi-rotor UAV platforms, which can be predicted to be widely used in weather forecasting and aviation security tasks when they mature, pointing to a new direction for weather detection.

The next step in our research will present attitude compensation algorithms by examining the link between UAV flying attitude and wind measurement accuracy. Additionally, we will conduct more research on the WPOD anemometer's performance in a large wind tunnel.

Author Contributions: T.H.: conceptualization, methodology, software, writing—original draft. H.X.: supervision. W.G.: data curation, software. X.L. and H.L.: validation, formal analysis. H.Z.: writing—review and editing. All authors have read and agreed to the published version of the manuscript.

Funding: This research was supported by the National Key Research and Development Program of China (grant number 2021YFE0105500), the National Natural Science Foundation of China (grant number 62171228) and the Jiangsu Province Graduate Research Innovation Plan (grant number KYCX22_1195).

Data Availability Statement: The data that support the findings of this study are available on request from the author, [T.H.], upon reasonable request.

Acknowledgments: The authors would like to thank the Nanjing University of Information Science and Technology.

Conflicts of Interest: The authors declare that they have no known competing financial interest or personal relationships that could have appeared to influence the work reported in this paper.

References

1. Jozef, G.; Cassano, J.; Dahlke, S.; de Boer, G. Testing the efficacy of atmospheric boundary layer height detection algorithms using uncrewed aircraft system data from MOSAiC. *Atmos. Meas. Tech.* **2022**, *15*, 4001–4022.
2. Vincent, V.; Chiu, E.; Tae, K.S.; Bukhori, I.; Setiyadi, S. Automatic Wireless Mobile Weather Station. *J. Electr. Electron. Eng.* **2020**, *2*, 54–59. [[CrossRef](#)]
3. Rodríguez, O.; Bech, J.; Soriano, J.d.D.; Gutiérrez, D.; Castán, S. A methodology to conduct wind damage field surveys for high-impact weather events of convective origin. *Nat. Hazards Earth Syst. Sci.* **2020**, *20*, 1513–1531.
4. Kim, J.h.; woo Lee, D.; Cho, K.r.; Jo, S.y.; Kim, J.h.; Min, C.o.; Han, D.i.; Cho, S.j. Development of an electro-optical system for small UAV. *Aerosp. Sci. Technol.* **2010**, *14*, 505–511. [[CrossRef](#)]
5. Rautenberg, A.; Graf, M.S.; Wildmann, N.; Platis, A.; Bange, J. Reviewing wind measurement approaches for fixed-wing unmanned aircraft. *Atmosphere* **2018**, *9*, 422.
6. Lehner, M.; Whiteman, C.D.; Hoch, S.W.; Jensen, D.; Pardyjak, E.R.; Leo, L.S.; Di Sabatino, S.; Fernando, H.J. A case study of the nocturnal boundary layer evolution on a slope at the foot of a desert mountain. *J. Appl. Meteorol. Climatol.* **2015**, *54*, 732–751. [[CrossRef](#)]
7. Kalverla, P.C.; Duine, G.J.; Steeneveld, G.J.; Hedde, T. Evaluation of the Weather Research and Forecasting Model in the Durance Valley complex terrain during the KASCADE field campaign. *J. Appl. Meteorol. Climatol.* **2016**, *55*, 861–882.
8. Ma, S.; Wang, G.; Pan, Y.; Wang, L. An analytical method for wind measurements by a mini-aircraft. *Chin. J. Atmos. Sci.* **1999**, *23*, 377–384.

9. Zhang, Y.; Dong, T.; Liu, Y. Design of meteorological element detection platform for atmospheric boundary layer based on UAV. *Int. J. Aerosp. Eng.* **2017**, *2017*, 1831676. [[CrossRef](#)]
10. Johansen, T.A.; Cristofaro, A.; Sørensen, K.; Hansen, J.M.; Fossen, T.I. On estimation of wind velocity, angle-of-attack and sideslip angle of small UAVs using standard sensors. In Proceedings of the 2015 International Conference on Unmanned Aircraft Systems (ICUAS), Denver, CO, USA, 9–12 June 2015; pp. 510–519.
11. Witte, B.M.; Singler, R.F.; Bailey, S.C. Development of an unmanned aerial vehicle for the measurement of turbulence in the atmospheric boundary layer. *Atmosphere* **2017**, *8*, 195. [[CrossRef](#)]
12. Wenz, A.; Johansen, T.A. Estimation of wind velocities and aerodynamic coefficients for UAVs using standard autopilot sensors and a moving horizon estimator. In Proceedings of the 2017 International Conference on Unmanned Aircraft Systems (ICUAS), Miami, FL, USA, 13–16 June 2017; pp. 1267–1276.
13. Axisa, D.; DeFelice, T.P. Modern and prospective technologies for weather modification activities: A look at integrating unmanned aircraft systems. *Atmos. Res.* **2016**, *178*, 114–124.
14. Lawrence, D.A.; Balsley, B.B. High-resolution atmospheric sensing of multiple atmospheric variables using the DataHawk small airborne measurement system. *J. Atmos. Ocean. Technol.* **2013**, *30*, 2352–2366. [[CrossRef](#)]
15. Van den Kroonenberg, A.; Martin, T.; Buschmann, M.; Bange, J.; Vörsmann, P. Measuring the wind vector using the autonomous mini aerial vehicle M2AV. *J. Atmos. Ocean. Technol.* **2008**, *25*, 1969–1982. [[CrossRef](#)]
16. Xu, Q.; Wei, L.; Nai, K.; Liu, S.; Rabin, R.M.; Zhao, Q. A radar wind analysis system for nowcast applications. *Adv. Meteorol.* **2015**, *2015*, 264515. [[CrossRef](#)]
17. Susko, M. Jimsphere and radar wind profiler turbulence indicators. *J. Spacecr. Rocket.* **1994**, *31*, 678–683. [[CrossRef](#)]
18. Zhu, X.; Liu, J.; Bi, D.; Zhou, J.; Diao, W.; Chen, W. Development of all-solid coherent Doppler wind lidar. *Chin. Opt. Lett.* **2012**, *10*, 012801.
19. Bian, Z.; Huang, C.; Chen, D.; Peng, J.; Gao, M.; Dong, Z.; Liu, J.; Cai, H.; Qu, R.; Gong, S. Seed laser frequency stabilization for Doppler wind lidar. *Chin. Opt. Lett.* **2012**, *10*, 091405. [[CrossRef](#)]
20. Nuijens, L.; Siebesma, A.P. Boundary layer clouds and convection over subtropical oceans in our current and in a warmer climate. *Curr. Clim. Chang. Rep.* **2019**, *5*, 80–94. [[CrossRef](#)]
21. Wetz, T.; Wildmann, N.; Beyrich, F. Distributed wind measurements with multiple quadrotor unmanned aerial vehicles in the atmospheric boundary layer. *Atmos. Meas. Tech.* **2021**, *14*, 3795–3814. [[CrossRef](#)]
22. González-Rocha, J.; Woolsey, C.A.; Sultan, C.; De Wekker, S.F. Sensing wind from quadrotor motion. *J. Guid. Control Dyn.* **2019**, *42*, 836–852. [[CrossRef](#)]
23. Crowe, D.; Pamula, R.; Cheung, H.Y.; De Wekker, S.F. Two supervised machine learning approaches for wind velocity estimation using multi-rotor copter attitude measurements. *Sensors* **2020**, *20*, 5638. [[CrossRef](#)] [[PubMed](#)]
24. Allison, S.; Bai, H.; Jayaraman, B. Wind estimation using quadcopter motion: A machine learning approach. *Aerosp. Sci. Technol.* **2020**, *98*, 105699. [[CrossRef](#)]
25. Riddell, K.D.A. *Design, Testing and Demonstration of a Small Unmanned Aircraft System (SUAS) and Payload for Measuring Wind Speed and Particulate Matter in the Atmospheric Boundary Layer*; University of Lethbridge: Lethbridge, AB, Canada, 2014.
26. Wolf, C.A.; Hardis, R.P.; Woodrum, S.D.; Galan, R.S.; Wichelt, H.S.; Metzger, M.C.; Bezzo, N.; Lewin, G.C.; de Wekker, S.F. Wind data collection techniques on a multi-rotor platform. In Proceedings of the 2017 Systems and Information Engineering Design Symposium (SIEDS), Charlottesville, VA, USA, 28 April 2017; pp. 32–37.
27. Abichandani, P.; Lobo, D.; Ford, G.; Bucci, D.; Kam, M. Wind measurement and simulation techniques in multi-rotor small unmanned aerial vehicles. *IEEE Access* **2020**, *8*, 54910–54927. [[CrossRef](#)]
28. Mallon, C.J.; Muthig, B.J.; Gamagedara, K.; Patil, K.; Friedman, C.; Lee, T.; Snyder, M.R. Measurements of ship air wake using airborne anemometers. In Proceedings of the 55th AIAA Aerospace Sciences Meeting, Grapevine, TX, USA, 9–13 January 2017; p. 0252.
29. Thorpe, R.L.; McCrink, M.; Gregory, J.W. Measurement of unsteady gusts in an urban wind field using a uav-based anemometer. In Proceedings of the 2018 Applied Aerodynamics Conference, Atlanta, GA, USA, 25–29 June 2018; p. 4218.
30. Palomaki, R.T.; Rose, N.T.; van den Bossche, M.; Sherman, T.J.; De Wekker, S.F. Wind estimation in the lower atmosphere using multirotor aircraft. *J. Atmos. Ocean. Technol.* **2017**, *34*, 1183–1191. [[CrossRef](#)]
31. Li, Z.; Hu, H.; Shen, Y. The influence of rotor rotation of hexacopter on wind measurement accuracy. *J. Exp. Fluid Mech.* **2019**, *33*, 7–14.
32. Li, Z.; Pu, O.; Pan, Y.; Huang, B.; Zhao, Z.; Wu, H. A Study on Measuring the Wind Field in the Air Using a multi-rotor UAV Mounted with an Anemometer. *Bound.-Layer Meteorol.* **2023**, *188*, 1–27. [[CrossRef](#)]
33. Donnell, G.W.; Feight, J.A.; Lannan, N.; Jacob, J.D. Wind characterization using onboard IMU of sUAS. In Proceedings of the 2018 Atmospheric Flight Mechanics Conference, Atlanta, Georgia, 25–29 June 2018; p. 2986.
34. Hou, T.; Xing, H.; Yang, L. Orthogonal wind pressure vector decomposition wind measurement method based on multi-rotor UAV. *Chin. J. Sci. Instrum.* **2019**, *40*, 200–207.
35. Menter, F. Zonal two equation kw turbulence models for aerodynamic flows. In Proceedings of the 23rd Fluid Dynamics, Plasmadynamics, and Lasers Conference, Orlando, FL, USA, 6–9 July 1993; p. 2906.

36. Wang, L.; Hou, Q.; Wang, J.; Wang, Z.; Wang, S. Influence of the inner tilt angle on downwash airflow field of multi-rotor UAV based on wireless wind speed acquisition system. *Int. J. Agric. Biol. Eng.* **2021**, *14*, 19–26. [[CrossRef](#)]
37. Nguyen, D.T.; Choi, Y.M.; Lee, S.H.; Kang, W. The impact of geometric parameters of a S-type Pitot tube on the flow velocity measurements for greenhouse gas emission monitoring. *Flow Meas. Instrum.* **2019**, *67*, 10–22. [[CrossRef](#)]

Disclaimer/Publisher’s Note: The statements, opinions and data contained in all publications are solely those of the individual author(s) and contributor(s) and not of MDPI and/or the editor(s). MDPI and/or the editor(s) disclaim responsibility for any injury to people or property resulting from any ideas, methods, instructions or products referred to in the content.